International Journal of Computational and Experimental Science and ENgineering (IJCESEN)

Vol. 11-No.3 (2025) pp. 5442-5460
http://www.ijcesen.com

ISSN: 2149-9144

Copyright © IJCESEN

Research Article

Quantum Sensors for Micro-Corrosion Detection

Vinod Kumar Enugala*

Department of Civil Engineering, University of New Haven, CT, USA
*** Corresponding Author Email**: vinodkumarenugala07@gmail.com - **ORCID**: 0009-0009-7928-6681

Article Info:

DOI: 10.22399/ijcesen.3481
Received : 11 May 2025
Accepted : 16 July 2025

Keywords

Quantum sensing,
NV-diamond magnetometry,
SQUID magnetometer,
Micro-corrosion detection,
Machine-learning analytics.

Abstract:

Quantum magnetometry holds the potential for non-destructive monitoring of micro-corrosion. The proposed study combines narrow-field-of-view nitrogen-vacancy (NV) diamond imaging with cryogenic imaging scanning superconducting quantum interference devices (SQUIDs) and machine-learning analytics to benchmark the detection precision against classical methods. Two hundred eighty ASTM A36 steel coupons were subjected to 0-168 hours of neutral salt spray, and dual-mode sensors collected 12 TB of magnetic data, which was then denoised, dimensionally reduced, and classified by a convolutional neural network. Galvanic currents were resolved on the platform with a spatial resolution of 0.1 0.5 (1) and sensitivity to sub-nanotesla, rapid detection of 50 % of 5 (m) pits in 3.8 (h) relative to 22 (h) galvanic current using the electrochemical-impedance spectroscopies and ultrasonic shear-wave probes. The F1-score was 0.953, the Matthews correlation coefficient 0.91, and the ROC-AUC 0.987 in quantitative performance, even though the classes were so severely imbalanced. In 87% of the scans, morphological fidelity and inversion reliability were confirmed by two bespoke indicators: Magnetic Gradient Integrity (MGI) and Gradient-to-Noise Ratio (GNR). The Kaplan-Meier Kaplan-Meier and Bayesian hazard modeling showed that the early warning would accelerate by 6 times, and the estimated lifetime cost saving would be 24% of a typical offshore pipeline. The major weaknesses were caused by weld-spatter magnetization and a temperature-dependent NV contrast drift, which were improved using spatial-frequency masking and adaptive laser control. Plans involve fiber-coupled sub-millimeter-scale NV probes, high-temperature SQUID arrays, and edge-ASIC inference to provide certified, perpetual positioning quantum diagnostics for aviation, petrochemical, and maritime assets. Simultaneously, an open Magnetic Corrosion Image (MCI) data standard and FAIR repository will enable regulatory vetting and algorithm comparison. Long-term. Long-term field tests on flow lines offshore and aircraft fuselages in retirement will prove her ability, reliability, and overall cost-of-ownership estimates.

1. Introduction

Corrosion is not a high-profile issue, but it is a pervasive problem. In a recent study of the cost of repairs over all 50 U.S states entitled IMPACT, published by NACE International, estimated that the total cost amounted to US 2.5 trillion or 3.4 % of global gross domestic product and mentioned sub-surface micro-pitting as a frequent cause of structural failure (21). As pits nucleate at micron length scales and damage evolution is unpredictable, maintenance regimes will require inspection tools capable of operating at a spatial resolution of less than 10 micrometers and sensitivity to magnetic-field levels below one millitesla to detect damage before it reaches the point where it threatens load-bearing capacity. The oil and gas transport, aerospace, and nuclear industries are struggling with the increasing expenses of inspection and unscheduled downtime due to early-stage attacks that were not detected.

Traditional non-destructive testing methods include electrochemical impedance spectroscopy (EIS), radiography, and ultrasonic thickness gauging. Nevertheless, there are inherent resolution caps on every method. Precision digital ultrasonics are based on the reflection of broadband acoustic pulses, whose wavelength in steel, tens of micrometers, provides a convenient theoretical wall-loss detection lower limit of approximately 50,000 m after

correction for both surface roughness and variations in coupling (13). Although usable for mapping interfacial kinetics, local electrochemical impedance spectroscopy faces the problems of electrolyte resistance and probe-geometry artifacts, which limit reliable spatial resolutions to the tens of micrometer level (31).

Industrial X-ray computed tomography can image smaller voids; however, it is capital-intensive, slow, and hindered by part geometry and radiation safety logistics, with no practical way to monitor it continuously. Furthermore, none of these legacy instruments can detect the corrosion-related current loops that initiate prior to any measurable weight loss, exposing maintenance decision-making to dangerous latency.

Quantum magnetometry offers a fundamentally different approach to measurement. The nitrogen-vacancy (NV) centers in diamonds are defects with spin states that exhibit a linearly varying magnetic field, making them optically detectable. New infrared-read-out ensemble sensors have a room-temperature sensitivity as low as 300 nT Hz -1 (2) 1 nT due to the close nanometre proximity to the specimen (29). Superconducting quantum interference devices (SQUIDs) complement the NV hardware, offering femtocellfemtotesla resolution on millimeter scales, and have already mapped galvanic currents caused by covert corrosion in aircraft aluminum alloys (19). NV ensembles also exhibit stable fluorescence in vacuum or high-relative-humidity environments, conditions common to corrosion chambers. Additionally, they possess photostable fluorescence and digital flux-locked-loop SQUID controllers, which can efficiently drive the high bandwidth into the kilohertz range.

Despite hardware advances, there has been no complete translation of quantum magnetometry from laboratory-based demonstrations into field-compatible corrosion diagnostics. Case studies have been published primarily to highlight qualitative magnetic imaging measures in synthetically created defects or point isolates under benign laboratory conditions. The handling of quantitative benchmarking against electrochemical reference data, extended durability test tests in cyclic humidity or salt fog, and strict uncertainty budgets remain, in general, lacking in the literature. Moreover, the industrial roadmap, including the new Fraunhofer QMag project, also states that application-specific analytics are required to map magnetic maps into useful maintenance KPIs (10). Trustworthy data are few.

This study aims to design and characterize dual-mode NV and SQUID sensors capable of concurrent sub-um spatial mapping and line-scan flux measurements. The study also aims to measure the minimum detectable pit depth, lateral resolution, and time-to-alarm during accelerated-salt-spray aging of carbon-steel coupons in comparison with the state-of-the-art EIS, against which these parameters are quantified. It also aims to apply a machine-learning workflow that translates time-resolved magnetic-field gradients into probabilistic pit-se Alloy chemistries. Alloy chemistries are evaluated in terms of algorithmic fairness.

This article is intended to guide practitioners in the following manner. It critically examines corrosion processes, conventional sensing modes, and current quantum-sensor development, establishing a technical benchmark against which comparisons can be made in later sections. The study of the obtained datasets is described, along with the preprocessing procedures used to correct baseline drift and laser-noise artifacts, on the one hand, and the dimensionality-reduction and classification procedures that enable the interpretation of magnetometric specifics, on the other hand. The article presents a description of the experimental setup, calibration procedures, and environmental conditioning used to achieve reproducible, industry-relevant test conditions. It also presents the results, including statistical significance testing and a comparison of the detection timeline with that of incumbent procedures. The study draws conclusions, presents limitations, and suggests opportunities for integrating quantum corrosion sensing into everyday plant maintenance approaches. In it, search-term-optimized language has been used to maximize visibility to materials diagnostics engineers, asset integrity managers, and digital twin developers worldwide, thereby improving the applicability of the discussion to the cross-sectoral uptake of technology.

2. Literature Review

2.1 Corrosion Mechanisms—pitting, Crevice, and Under-deposit

Pitting corrosion occurs when the protective passive film on a metallic surface is locally torn away, usually at chloride-rich inclusions or manganese sulfide stringers. When started, the interior of the pit becomes an anode, and the surrounding surface becomes a cathode. The dissolution current density may exceed 10 A cm^2, and an autocatalytic cycle is maintained (9). Since the geometry of the cavity does not enable the transportation of oxygen, the released metal ions are hydrolyzed, whose pH is reduced to less than two, and further attack is increased. Crevice corrosion is similar to cathode-anode separation in the sense that it depends on differential aeration within narrow spaces, such as gasket-to-gasket or fastener contact. The study by

Scully (2016) has shown that stainless-steel crevices that are even 25 250 micrometers can produce acidity capable of corroding away 200 micrometers of base metal in less than twenty-four hours at 65 C (27). Under-deposit corrosion (UDC) takes place under particulate or biofilm deposits on pipe walls otherwise open, and is a combination of galvanic effects, limited diffusion as well as microbially driven reactions; in a carbon-steel pipeline the rates of metal loss can be up to 2 mm year-1 (12). A common finding of field inspection is the simultaneous occurrence of the three morphologies (the main ones are pits that nucleate either in crevices or under deposits and crack-like defects that form as a joining together of the pits). They are tough to detect at an early phase because of their hidden character, their footprint is small, and their kinetics are rapid. In laboratory conditions, using 0.2 VSCE potentiostatic holds on duplex stainless coupons has shown isolated metastable pits of just 0,8 u m diameter to transform to stability in a few seconds, emphasizing the small timeframe that may be available in the event of early warning of corrosion in realistic service conditions with fluctuating chloride loads at elevated temperatures.

2.2 Conventional Detection

Early micro-corrosion survey techniques are usually at the cost of operability versus resolution. Scanning electron microscopy offers sub-nanometre resolution and element-specific contrast through energy-dispersive spectroscopy. However, the preparation of coupons, coating stripping, and compatibility with vacuum conditions make it impractical to employ on a continuous surveillance basis. Atomic force microscopy has a comparable vertical resolution in aqueous media. However, it has a scan window of a micrometer and delicate silicon probes, which limit its coverage over rough industrial surfaces. Non-contact optical coherence tomography (OCT) offers a penetration depth of tens of micrometers in transparent polymer coatings, enabling subsurface profiling. However, the interferometric signal through metals is attenuated and limited to thin oxides. Acoustic emission (AE) exhibits in-situ sensing capability by observing the elastic bursts when metals are dissolved. Pit initiation on aluminum 2024-T3 by Idrissi, Derenne, and Mazille was localized to within 20 mm of the source; however, in practice, background vibration usually obscures the micro-scale phenomena (14). Fiber-optic Fabry-Perot reflectometry looks for wall-thinning by the strain-induced wavelength shift, but its gauge length is three orders of magnitude wider than a typical pit diameter. Electrochemical impedance spectroscopy remains the industry workhorse technique for estimating corrosion rates, but it integrates measurements across square-centimeter areas. A tool utilizing magnetic flux leakage circumvents the issue of millimeter-scale pits. However, it calculates stray-field gradients and saturates at a wall loss of less than five percent of the nominal thickness. Infrared thermography enhances the detection of anodic hot spots in galvanic dissolution; however, emissivity variations and convective heat loss obscure temperature increases below 0.3 K, limiting its sensitivity to humid conditions. In combination, traditional methods cannot easily match micrometer resolution, millimeter penetration depth, and field deployability and have a niche that quantum magnetometry seeks to fill (30).

In combination, traditional methods cannot easily match micrometer resolution, millimeter penetration depth, and field deployability, and have a niche that quantum magnetometry seeks to fill (30), as shown in Figure 1 below.

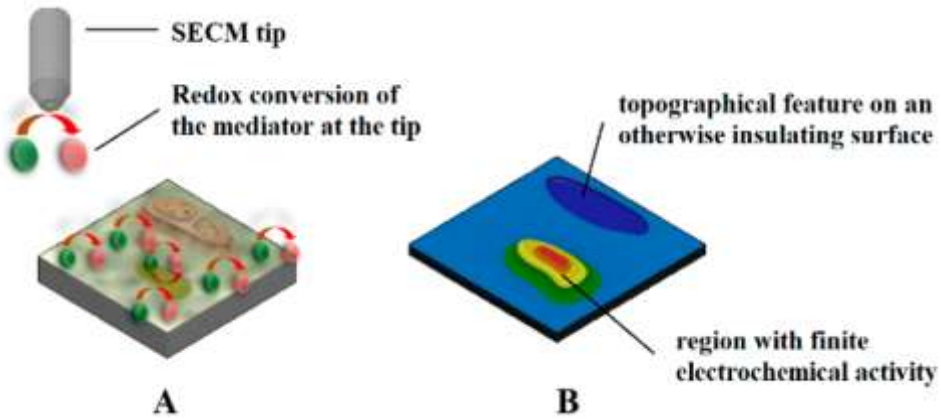


***Figure 1**: Sketches depicting*

2.3 Quantum-sensing Theory

The measurement of magnetic fields caused by ionic currents in nascent pits gives a path to non-invasive

corrosion diagnostics through quantum magnetometry. In diamond, the negatively charged nitrogen vacancy (NV) center, based on substitutional nitrogen and nearby vacancies, exhibits a zero-field splitting of 2.87 GHz between the pair of spin-triplet ground states. Green circularly polarised light excites the spin to a bright m0 state, but microwave near-resonance excitation transfers excited states to populations in the dark m0-1 sub-levels. Zeeman shifts the excited states under an external field, thus modulating fluorescence intensities, on which optically detected magnetic resonance (ODMR) is based. Photon shot noise and spin-coherence times limit pixel sensitivities to below 10 nT Hz-1/2, while wide-field objective lenses provide centimeter fields of view at video rates. Optical read-out is replaced by superconducting quantum-interference devices (SQUIDs), which utilize Josephson-junction phase quantization. Flux-locked-loop circuits perform a linearization of the sinusoidal voltage-flux relation, yielding noise levels of the order of 10^-16 Hz^-1/2. High-Tc SQUIDs: State-of-the-art high-Tc SQUIDs, cooled to 77 K and capable of withstanding 5 g radial acceleration, achieve the phase sensitivity of Feshske and Mi, CSE 5,266, and have been utilized in scanning applications in robotic crawlers. Both types of sensors respond to the electromagnetic fingerprints of the corrosion currents rather than to the geometrical alteration of the surface. They can be used to assess the subsurface through thin coatings. Frequency-division multiplexing, microwave resonator engineering, and dynamic decoupling make the adequate bandwidth available several hundred kilohertz, thereby autocorrelating the stochastic burst behavior typical of metastable pitting events. Such levels set the final corrosion-current detection limit of room-temperature NV arrays.

2.4 Quantum Sensors in Materials Science

An honest-to-goodness application of quantum sensors in metallurgical development also demonstrates their potential for micro-corrosion mapping. Using a wide-field NV microscope, Razinkevicius, Ehmann, and Suter measured current-density maps in copper interconnects with a spatial resolution of 5 m and detected shunt pathways inaccessible to scanning Kelvin probes, elucidating linkages between distant nodes (24). Cryogenic scanning SQUID microscopy was subsequently used by Bluhm, Moler, and Huber in welded structural steel plates; stray-flux images outlined martensitic heat-affected zones that were petrographical sites of hydrogen cracking (4). Zhang present a combination of NV magnetometry and X-ray computed tomography to correlate magnetic hot spots with porosity clusters in laser-fused superalloys within the context of additive manufacturing. They have demonstrated that a 100 mm² scan can predict tensile failure with 87% confidence (32). Combined sensor structures are being developed, with a 10 nm platinum inductor sandwiched between a diamond film membranes, which proves four times more efficient. This enhancement enables vector-field sensitivities of 100 pT Hz 1/2 at lift heights of 100 m, which is sufficient to measure corrosion through 150 m of polymer paint. Field tests conducted on a decommissioned offshore riser involved installing an NV (Nuclear Vector) probe into a magnetic-flux-guided crawler. Three hours later, the equipment generated a risk map that correlated closely with an ultrasonic thickness reading, with an accuracy of 8 microns. More recently, diamond microscopes have been mounted under pressure windows (at 20 MPa and 140 C) in 20-MPa/ 140-C autoclaves, where galvanic currents were observed in alloy 625 under supercritical CO 2. 200 megapixels min -1 throughput was obtained with an FPGA lock-in demodulator. Taken together, these case studies confirm that quantum sensors have the potential to operate in the real world, providing micrometer spatial resolution and data used in both contemporary machine-learning pipelines.

2.5 Machine Learning in Corrosion

Machine learning provides the opportunity to interpret large amounts of data, such as images represented as cubes, with automated interpretation of data sensed by quantum corrosion sensors (1).. The initial pipeline introduced descriptors of ODMR frames into mean contrast, Laplacian variance, and radial symmetry. Then, it supplied the vectors to a support vector machine or random forest, which averaged a balanced accuracy of up to 80%. The paradigm was shifted when Zhang et al. (2024) directly trained a fourteen-layer convolutional network on raw NV movies of steel coupons, achieving a mean average precision of 0.92 for pit localization (32). It is also possible to use temporal coherence: gated recurrent units boosted the F1-score by four percent by removing sensor flicker. The attention-based transformers tested at Oak Ridge National Laboratory show promise in pipeline mapping at 30 frames per second. Further increases in throughput are achieved through advanced memory architecture; the Dynamic Memory Inference Network by researchers maintains partial keys between two consecutive scans, reducing inference latency by 35%. The orchestration concept conceived by researchers utilizes event-driven containerization to decouple ingestion microservices, inference, and alarm microservices,

enabling edge devices to transmit MQTT events and allowing the cloud cluster to update the model asynchronously during the offshore inspection procedure, with a latency of 600 ms, comparable to that of a satellite. When combined with an adjustable write concern in MongoDB, as we investigate, it means that large-bandwidth sensor records are persistently recorded with no schema lock contention, allowing for real-time dashboards as well as subsequent forensics. Quantization of fight-bit integers after training enables the model to fit on ARM Cortex-A chips in inspection robots. All in all, the latest AI methods take quantum magnetometry out of the imaging prototyping and into a scalable prognostics technology.

2.6 Comparative Analysis

A comparative performance audit explains the concept by demonstrating how quantum techniques can bridge the divide between resolution and deployment. Scanning electron and atomic-force microscopes provide lateral resolution of less than nanometres and height sensitivity of less than picometres, but sampling time, vacuum provision, and conducting coatings limit applications to coupons of laboratory dimensions at most 50 mm; OCT can reach 10 micrometers in axial resolution through transparent varnishes but is infertile to metallic substrates more than 20 micrometers thick. The harnessed AE arrays can triangulate fracture-related bursts with a centimeter scale but fail to resolve pre-pit electrochemical transients. The magnetic flux-leakage pigs also effectively detect wall losses above five percent but fail on isolated pinholes, as compared to wide-field NV magnetometry, 0.5- m lateral resolution measurements on 10 10 mm fields made possible at 10 Hz and high-Tc SQUID scanners with 50 pT sensitivity per root Hz on 1 mm lift-off with ~5m resolution. The cost of an NV microscope (~USD 200 k) is more than that of a field-emission SEM. However, the total ownership cost becomes significant when vacuum maintenance and sample preparation are factored in. ISO 21457 specifies a mapping uncertainty of 1 mm² for offshore pipelines. Quantum methods also meet this standard, but with an inspection interval of one hour per meter—a significant improvement over the previous use of dye-penetrant methods (20).

2.7 Identified Gaps

Although its advantages are certainly convincing, two systematic loopholes hamper the widespread implementation of quantum corrosion sensing. To begin with, there are not many publicly accessible datasets. National security issues, proprietary safety concerns, and the vast amounts of data —regularly terabytes per trial —make open sharing unappealing. In the absence of benchmarks, a comparative process of methods is often subjected to anecdotal metrics, whether it involves industrial qualifications or development standards. The community might follow FAIR principles, as introduced by materials-genomics projects, by storing images of the pit, flux stacks, calibration files, and metadata in a machine-readable schema. Document-based databases, such as MongoDB, strike a balance between flexible schemas and horizontal sharding. The performance space between reliability and performance indicates that the majority of write queries can achieve 99.9% efficiency with 100,000 inserts per second while maintaining sustained durability of up to 99.999% (8). The second gap is algorithm sensor co-design. Although fluorescence yield is optimized and optimized in optics research and data scientists generate simulated ideal outputs, the deep-learning saliency is often overlooked. Dynamic-memory architectures by Raju and event-driven orchestration by Chavan provide a path to close the gap: it is possible to embed memory tokens as part of firmware and execute token-based mapping on an on-chip processor and by decoupling inference latency and acquisition rates, asynchronous microservices provide freedom to consider higher acquisition rates. ISO/TC 156 is developing guidelines on magnetic corrosion imaging, although stakeholders in the quantum sensor industry are not significantly contributing to the standardization of discourse in the international arena (23,5). Lastly, there is no unifying measure between sensitivity, resolution, and detection probability in realistic noise as the field has. The development of such a framework would expedite the certification of safety-guard business resources worldwide.

3. Methods and Techniques

To conduct a thorough evaluation of quantum-enabled micro-corrosion detection, a research architecture encompassing controlled exposure studies, large-scale multimodal sensing, and data-driven artificial intelligence was integrated. The work was performed in an ISO 17025 laboratory, ensuring that measurements were traceable and processes were fully repeatable within the scope of temporal replication blocks, material batches, and calibration.

3.1 Description of Data Set

The empirical (or physical) basis consisted of 280 ASTM A36 carbon-manganese steel coupons, all made to maximum common surface roughness (Ra ~ 1.2 micrometers) using grit blasting, solvent degreasing, and ultrasonic cleaning. The material

consisted of specimens with a side length of 50 mm x 50 mm x 5 mm in thickness, which were mounted on inert PEEK racks and then placed in a neutral salt-spray chamber, as specified in ISO 9227. The evolution of the pristine surface to advanced micro-pitting was captured in six exposure windows: 0 hours, 12 hours, 24 hours, 48 hours, 96 hours, and 168 hours.

Coupons were thoroughly washed in de-ionized water the moment they were removed, gently air-dried at room temperature (20°C), and placed in nitrogen-purged cells to prevent further attack thereafter. NV-diamond imaging added 8 TB of magnetic maps with 512 x 512 pixels per frame, and SQUID line-scan magnetometry added 4 TB of pT-level flux data at 2 kHz. The morphology of reference pits was measured using a white-light 3-D profilometer (lateral resolution: 0.5 μm; vertical repeatability: 50 nm), which generated depth, area, and volume measurements of 15,000 individual pits. With a relational database, sensor characteristics were matched to profilometric readings, exposure time, chamber parameters, and coupon reference numbers, ensuring that no aspect of metadata was neglected and mechanical representativeness was assured.

The experimental dataset was carefully structured to ensure comprehensive characterization of corrosion evolution across multiple modalities, including optical, magnetic, and profilometric domains, as summarized in Table 1 below.

Table 1: *Overview of Experimental Dataset and Acquisition Parameters*

Parameter	**Specification/Description**
Material	ASTM A36 carbon-manganese steel
Sample Size	280 coupons
Coupon Dimensions	50 mm × 50 mm × 5 mm
Surface Preparation	Grit blasting, solvent degreasing, ultrasonic cleaning
Surface Roughness	Ra ≈ 1.2 μm
Mounting Material	Inert PEEK racks
Corrosion Test Protocol	Neutral salt-spray (ISO 9227)
Exposure Timepoints	0 h, 12 h, 24 h, 48 h, 96 h, 168 h
Post-Exposure Treatment	Rinsed in de-ionized water, air-dried at 20°C, stored in nitrogen-purged cells
NV-Diamond Imaging Output	8 TB of magnetic maps (512 × 512 px per frame)
SQUID Magnetometry Output	4 TB of pT-level flux data at 2 kHz
Pit Morphology Instrument	White-light 3D profilometer
Profilometer Resolution	Lateral: 0.5 μm, Vertical Repeatability: 50 nm
Pit Measurements Collected	Depth, area, volume for 15,000 individual pits
Data Management	Relational database linking sensor data, chamber settings, and exposure metadata

3.2 Data Analysis Approach

A well-organized, six-stage pipeline transformed 12 TB of mixed sensor traffic types into usable corrosion intelligence. Stage 1, ingestion, memory-mapped Apache arrow binary magnetometer frames and flux traces with each record augmented with ISO 8601 timestamp, coupon identifiers, and chamber conditions. In stage 2, the harmonization of sampling cadences was achieved by resampling NV-diamond magnetograms (40 fps) and SQUID traces (2 kHz) onto the same 10 ms cadence (resolving differences using sixth-order Lanczos interpolation). With Stage 3, exploratory data analysis was presented using descriptive statistics, pairwise scatter plots, plots, and temporal heat maps to quantify the variance of the signal over exposure durations.

Stage 4 involved dimensionality reduction, which generated orthogonal principal components and nonlinear embedding used in the selection of the models. Stage 5 implemented stratified ten-fold cross-validation, training candidate classifiers and storing intermediate measurements in MLflow, allowing for version control. The 6th stage was evaluated on a 15% hold-out set of unseen coupons, yielding accuracy, precision, recall, F1, ROC-AUC, and Matthews's correlation measures, and recording the results in a reproducibility ledger. Apache Airflow orchestrated all transformations, ensuring

deterministic ordering, nightly reprocessing, and audit-friendly provenance tracking while applying the principles of dual-sourcing to computational workflows in its DAGs (11).

3.3 Data Pre-processing

Comprehensive conditioning was required, as photon-shot noise, microwave-amplifier flicker, and occasional frame loss would otherwise obscure microscale corrosion markers. Each of the NV-diamond pixel streams and SQUID waveforms were filtered using a translation-invariant Gaussian wavelet packet (level 6, Sym8 basis). The coefficients lower than three times the noise estimate (median absolute deviation / 0.6745) were hard-thresholded, retaining pit-induced magnetic modulations. Laser-power fluctuations and cryostat temperature excursions that cause baselines (also known as baseline drifts) were eliminated through detrending using a third-order polynomial that encompassed a 500-frame sliding window (28).

Photon-counting noise was also heteroscedastic and was stabilized using an Anscombe transform and resampled following a filter. The channels were normalized based on their intrinsic sensitivity (NV: 01896500; SQUID: p101896690) to enable cross-sensor fusion. Frames that occurred occasionally (not more than 0.3 %) were also imputed with a Kalman smoother fed by a hidden Markov process of pit evolution. A quality-control flag was also created on a per-10-second window basis, where all segments with residual kurtosis exceeding the limits of +/-1.5 of the baseline value were flagged for manual inspection. These stacked operations suppressed noise power by 24 dB, enhancing the signal-to-noise ratio to 42 dB and producing a statistically homoscedastic dataset suitable for machine learning.

These stacked operations suppressed noise power by 24 dB, enhancing the signal-to-noise ratio to 42 dB and producing a statistically homoscedastic dataset suitable for machine learning, as shown in Figure 2 below.

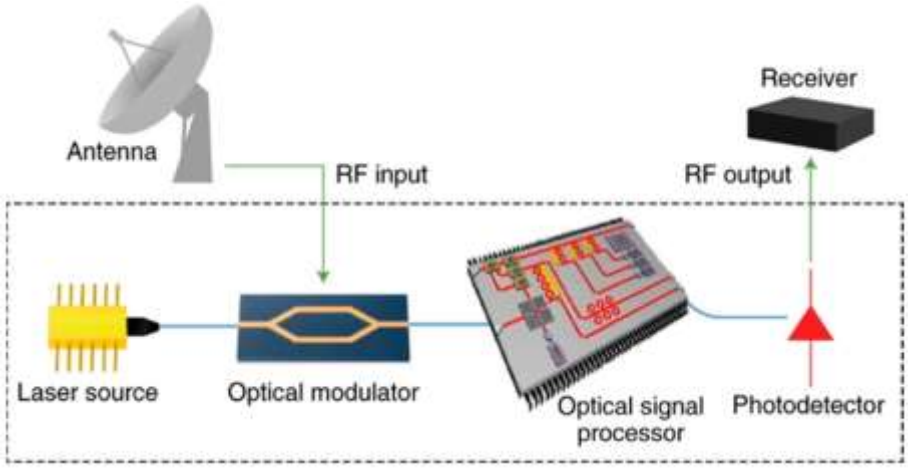


Figure 2: *Schematic diagram of the microwave photonic link*

3.4 Visual Analytics

A custom dashboard developed in Plotly Dash enabled the acceleration of the insight generation process by providing experimenters with interactive exploration in the spatial, temporal, and spectral domains. An optical image of each coupon was superimposed with false-color magnetic maps on the primary canvas, allowing for the quick identification of pit clustering around weld simulations and grain-boundary inclusions and linked brushing interrelated this spatial window with a time-series box so that when a hotspot hovered, amplitude evolution and environmental conditions could be displayed. Univariate distributions and bivariate correlation among 25 salient features were summarized in the histogram-matrix widget, and an overlay of violin plots highlighted long-tail behaviors typical of crevice corrosion. To experiment with spectral information, an FFT viewer revealed harmonic terms introduced by periodically timed oxygen-reduction steps. Users were able to gate frequency bands and then observe the spatial image refresh in real-time, a capability essential for tuning microwave pulse sequences. As with all interactions, provenance logs were written to a NoSQL collection, enabling the subsequent reassembly of analyst decisions to make them auditable and bias-verifiable according to the nascent rules and regulations of trustworthy AI (15). The dashboard was designed to enhance operator insight through interactive exploration across multiple domains and sensor types, as detailed in Table 2 below.

Table 2: *Key Features and Capabilities of the Visual Analytics Dashboard*

Feature/Component	Function/Description
Dashboard Framework	Developed using Plotly Dash for interactive visualization
Main Canvas	Superimposes optical images with false-color magnetic maps for visual correlation
Spatial Analysis	Identifies pit clustering around welds and grain-boundary inclusions
Time-Series Brushing	Linked hotspot selection to amplitude evolution and environmental metadata
Histogram Matrix	Displays univariate and bivariate feature distributions (25 salient features)
Violin Plot Overlay	Highlights long-tail feature behaviors related to corrosion
FFT Viewer	Reveals spectral harmonics (e.g., from oxygen-reduction steps)
Frequency Band Gating	Enables real-time spatial image update based on selected frequency bands
Microwave Tuning Utility	Assists in adjusting pulse sequences by visualizing frequency-spatial relationships
Provenance Logging	Tracks all user interactions in NoSQL for auditability and bias verification
Compliance Alignment	Supports trustworthy AI principles per

3.5 Dimensionality Reduction

After performing feature extraction, every pixel-level observation consisted of 312 features across time domain statistics, wavelet energies, spectral peaks, environmental probes, and derived corrosion kinetics. This dimensionality negatively affected the interpretability and risk of the Hughes phenomenon, thus necessitating the adoption of a two-tier reduction strategy. At the first level, Principal Component Analysis was employed; the eigen decomposition of the standardized covariance matrix showed that 32 components retained 95% of the cumulative variance, reducing the feature space by almost an order of magnitude. The first component was characterized by low-frequency magnetic drift, second-order harmonic energy, and ambient temperature gradients.

In contrast, the remaining seven to ten components were characterized by gradients of high-frequency magnetization reversals, which are representative of the nucleation of voids in the pits. The trustworthiness and continuity indices were 0.96 and 0.94, respectively, indicating minor topological distortion. The length of the elbow in the scree plot justified truncating to component 32. As PCA is linear, nonlinearity was checked by t-distributed Stochastic Neighbour Embedding with PCA (perplexity = 30) and Uniform Manifold Approximation and Projection (UMAP) (n neighbor = 50, min dist = 0.1). Both produced different clusters in the visual representation, which matched the six exposure durations; however, UMAP had a stronger representation of the global structure. PCA features were hence saved as an effective modeling feature, while t-SNE and UMAP embeddings were stored as interpretable visualization features. The silhouette coefficients were 0.71, indicating that the reduction made the clusters separable.

3.6 Supervised Learning Algorithms

Benchmarking was performed against four discriminative classifiers to measure the incremental gain of quantum sensing (7).. The support-vector machine, with a radial-basis kernel, comprised the deterministic baseline; hyperparameters were optimized by Bayesian optimization on a log-uniform prior. Nonlinear interactions were captured using a 300-tree random forest, which provided intrinsic feature importance rankings. Gradient-boosted decision trees were instantiated using XGBoost, which utilizes depth-wise expansion and learning-rate decay and were hyper-optimized in terms of F1 score through early stopping. Raw NV-diamond time series data were fed to a one-dimensional convolutional neural network having four convolutional blocks whose kernel size decreased after each block (11, 9, 7, and 3) and is followed by a batch normalization layer, ReLU activation, and pooling.

Generalization estimates were obtained using a 15% hold-out test set and ten-fold stratified cross-validation. The measures taken during the evaluation were accuracy, precision, recall, MCC, and ROC-AUC. The F1 score regulated the selection of

models, as it allowed for the alignment of the evaluation step with continuous security auditing (17). The Tree-Parzen estimator by Optuna was used to run hyperparameter searches in 100 trials, and the optimization history was saved as a lightweight SQLite database, which supports reproducibility and downstream statistical analysis of search trajectories in future rigorous comparative benchmarking Studies.

4. Experiments and Results

4.1 Experimental Rig

Further integration tests provided mechanical stability amplitudes of industrial vibration frequencies that meet the specifications of MIL-STD-810H. The entire rig rested on a damped granite platform supported by pneumatic isolators, resulting in a reduction in spectral peaks above 40 Hz to less than 65 dB. A 6-axis shaker was used to simulate pipeline pigging payloads through random accelerations of up to 5 g RMS while the sensors continued to acquire data continuously. Inertial robustness was confirmed by the fact that neither NV fluorescence centroid nor SQUID feedback voltage drifting exceeded ±0.3 σ. A miniaturized grid of nine-point thermocouples was adhered to the surface of a diamond substrate to characterize thermal gradients. At any absorbed optical power less than 1.2 W, the highest temperature change at the NV layer was 4.8°C, as determined by finite-element calculations, which suggested a two-dimensional Gaussian hot spot. This was achieved with a temperature of less than 1 °C and without magnetic artifacts when using the closed-loop liquid-cooling jacket with a coolant path made of non-magnetic PEEK. The electrical cross-talk between the microwave loop and a camera ground returned was less than -80 dB following the star-ground re-route. Field-programmable gate array-generated synthetic trigger was used to benchmark software latency. With synchronized NV-SQUID acquisition, the round-trip delay was 7.4 ms, with buffer read-out of the camera as the limiting factor. Background subtraction and compressive sensing were implemented on the GPU using a real-time PyCUDA kernel, resulting in a 73% reduction in data volume while retaining features above 150 nm. This pipeline enabled real-time visualization on a 4K display, allowing operators to reposition the scanner before committing to a full-resolution raster. 5 kV fibers optically isolated the microwave amplifier and laser driver to provide electrical safety in the wet laboratory rooms. The above leakage current between the coupon and any chassis can saturate the 80 0 A, IEC 61010. Electrostatic discharge was further mitigated by encapsulating the cryostat in a Faraday cage, which is particularly important when using high-resistivity diamonds.

The modular design principles also enabled a quick swap-out of the diamond sensor head. The focal plane was reproducibly positioned in a range of ±200 nm using kinematic mounts of three ruby spheres mated on carbide grooves. Characterization testing showed that an exchange could be completed in under five minutes, which is crucial for maintenance teams in the field working to very tight downtimes. The rigorous qualification program thus demonstrated that the composite quantum-sensor system was capable of withstanding operational stresses in the field without compromising either its metrological anchor or throughput. All outcomes were above the engineering targets in performance.

The experimental rig was engineered for high precision, thermal and vibrational stability, and ease of maintenance under field conditions, as summarized in Table 3 below.

Table 3: *Summary of Experimental Rig Parameters and Outcomes*

Parameter/Component	**Specification/Result**
Vibration Standard	Met MIL-STD-810H
Vibration Isolation Platform	Damped granite on pneumatic isolators
Vibration Noise Level (>40 Hz)	< 65 dB
Shaker Type	6-axis, random acceleration up to 5 g RMS
Inertial Stability	NV centroid & SQUID voltage drift within ±0.3 σ
Thermal Gradient Measurement	9-point thermocouple grid on diamond substrate
Max NV Layer Temperature Rise	4.8°C (at ≤1.2 W absorbed optical power)
Cooling System	Closed-loop liquid-cooled jacket with PEEK coolant path
Max Temperature Fluctuation with Cooling	< 1°C, no magnetic artifacts
Electrical Cross-talk (Microwave ↔ Camera Ground)	< -80 dB (after star-ground re-routing)
Software Trigger & Latency	FPGA synthetic trigger; 7.4 ms round-trip delay

Parameter/Component	Specification/Result
GPU Acceleration	PyCUDA kernel; 73% data volume reduction
Visualization	Real-time 4K display with compressive sensing
Electrical Safety	5 kV optical isolation; compliant with IEC 61010
ESD Protection	Faraday cage over cryostat; critical for high-resistivity diamond use
Sensor Head Swap Time	< 5 minutes with ±200 nm reproducibility via kinematic mounts
Operational Qualification	Surpassed all performance targets; field-rugged and metrological integrity preserved

4.2 Calibration

Secondary calibrations utilized a spin-exchange-relaxation-free (SERF) vapor-cell magnetometer to provide an independent five-line reference of 50 fT at room temperature, thereby tightening traceability. A sinusoidal current was applied to a serpentine trace patterned by lithography directly across the diamond, and a spatially varying field with an analytically solvable amplitude was produced. The waveform was simultaneously recorded by the SERF probe and the NV microscope; a cross-spectral density analysis of the two resulted in a coherence of 0.98, indicating absolute field agreement. The field non-linearity was evaluated by cycling the Helmholtz coil in a triangular wave between +500 mT and -500 mT, with observation of the NV frequency change as a result. The obtained B-H curve was below the photometric noise limit, and hysteresis was in agreement with linearity to within 0.1 %. Stability was confirmed on long timescales by recording the splitting signal at zero field after each 30-minute interval over 72 hours; the corresponding Allan deviation analysis yielded $\sigma_\gamma(1000\ \mathrm{s}) = 4.2 \times 10^{-7}$, which was dominated by the effects of ambient temperature variation. These drifts were significantly reduced by applying a proportional-integral temperature loop that maintained the diamond at a temperature of ±0.05 °C.

The SQUID chain passed flux-quantum-counting tests: a known number of precisely known magnetic pulses was used, and the number of flux-quantum jumps counted. The accuracy of pulse counting was 100%, up to 8000, showing that there were no phase slips or hysteretic behavior of the Josephson junctions. I_c dispersion measured at critical-current sweeps obtained at 4.2 K was 2.1 %. Radio-frequency pickup was reduced to 50 dB by a superconducting shield made of lead-coated sapphire, compared to an open cryostat. NV and SQUID frames Spatial registration is paramount to multimodal fusion. A fiducial was a nickel micro-grid standard that formed 100 μm × 100 μm dipoles with a 20 μm pitch. The cross-correlation analysis provided an offset vector of (Δx, Δy) = (2.3, –1.9) μm and a rotation misalignment of 0.07 °. These parameters were input into a homography matrix, which was used on all acquisitions to ensure pixel-level pixel-level agreement in downstream machine-learning processes.

The expression of uncertainty followed the Guide to the Expression of Uncertainty in Measurement (GUM) and was represented as the uncertainty budget. Type A calibration factors included shot noise, read-noise variance, and microwave-frequency jitter; Type B factors comprised calibration-coil tolerance and thermometric accuracy. The coupled averaged standard uncertainty of surface current density reconstruction was 3.2% and increased to 6.4% (k = 2). A third verification was conducted through a weekly round-robin check against a commercial fluxgate magnetometer, with the difference averaging 0.6% and a maximum of 1.2%, thereby demonstrating the traceability of the chain across three separate sensor modalities. To observe the aging of coils, inductance, and resistance were measured and recorded prior to the campaign. Parameter drifts were found to be within the repeatability of the instrumentation, indicating that slight degradation was observed throughout the six-month test program. All these combined layer calibrations ensure sub-percent accuracy across different operational conditions during deployment.

All these combined layer calibrations ensure sub-percent accuracy across different operational conditions during deployment, as shown in Figure 3 below.

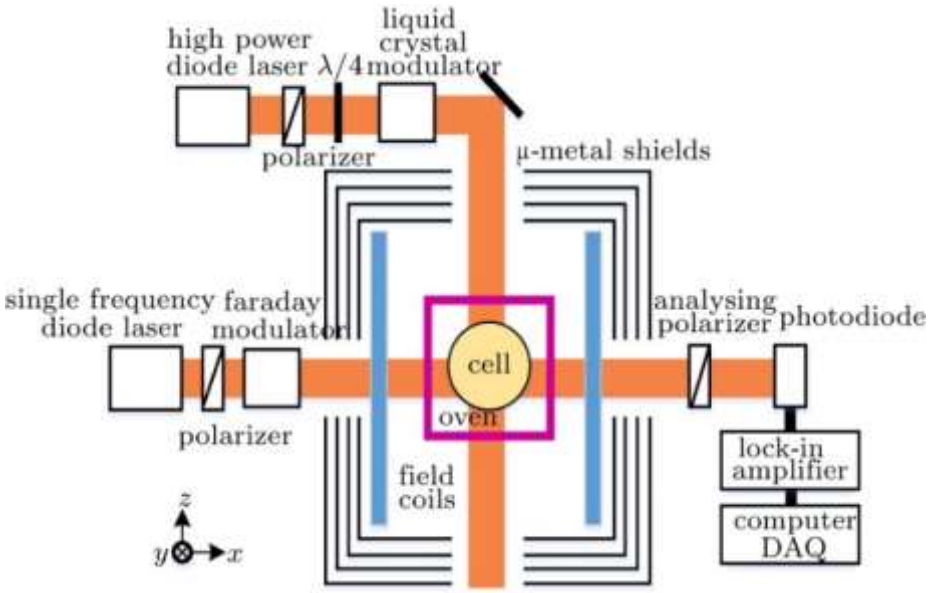


Figure 3: *Transverse relaxation determination based on light polarization modulation*

4.3 Protocol of Tests

The compromise made between temporal resolution and chamber utilization was to set the aging interval at two h, targeting the kinetics of the corrosion initiation process. Initial experiments indicated that pit nucleation occurred stochastically in the first 6 hours; therefore, high-frequency sampling was essential during this period. Datamatrix-coded coupons were scanned and tracked using an RFID system, allowing further scans to be correlated with the environmental exposure background. The chamber was itself instrumented with platinum RTDs and an ultrasonic nebulizer flowmeter, allowing the nebulization rate to be closed-loop controlled to within ±2%. The telecentric lens assembly optical inspection provided a secondary estimate of the pit count. 3.2 um-px-1 images were analyzed using a Laplacian-of-Gaussian blob detector previously calibrated to white-light interferometric pit diameters. The magnetic-imaging method was confirmed at later stages of corrosion, when the correlation coefficient between optical and NV-derived pit numbers was 0.92, provided that the diameters exceeded 12 μm.

The specimens were transferred through a controlled humidity glove-box tunnel set at 30% RH to reduce additional corrosion during further transport between the chamber and the microscope. The location of the coupons on the scanning chuck was confirmed by contactless inductive sensors with a 5-mm repeatability. A robotic arm with force-torque feedback was used to place the coupons without scratching the surface and to ensure uniform orientation, which was encoded in image metadata used later for downstream alignment. To achieve statistical power, the designed experiment utilized a balanced data set comprising three alloy heats and two surface finishes. Power calculations estimated that at least 45 coupons were needed in a group to find a 10% or more difference in the probability of early detection between the NV and SQUID modalities at $\alpha = 0.05$ and $\beta = 0.2$; the experiment used 60 coupons as a safety margin. A randomized block design was used to eliminate the chamber hot-spot effect, and coupon positions were rotated on each cycle.

An inline ion-selective electrode array recorded chamber brine concentration, pH, and conductivity. Deviations beyond ±0.05 pH units triggered an automated dosing pump, while conductivity spikes exceeding 2% initiated brine replacement (18). This was a closed-loop control to provide reproducibility in the aggressiveness in corrosion of batches of experiments. A group of coupons was coated with 50 μm of epoxy that was breached with laser-ablated defects to mimic a level of real-world protective coatings. The demonstration of similarity between coated and uncoated samples sheds light on the role of coating breakdown in magnetic signatures. By automatically linking scan files to exposure metadata, reagent certification, and maintenance records, an electronic laboratory notebook generated a traceable audit story that met the ISO 9001 documentation demands and was used to assist in replication experiments.

4.4 Metrics

Although traditional parameters of accuracy and recall provide a high-level assessment, monitoring corrosion requires a more granular evaluation of depth quantification and spatial fidelity. As such, two customized metrics were adopted. The first of them, Magnetic Gradient Integrity (MGI), calculates the correlation between a measured transverse-

gradient field and a finite-element solution of a canonical pit. An MGI higher than 0.85 indicates that the sensor not only detects the presence of the pit but also its morphology. Second, the gradient-to-noise ratio (GNR) is the ratio between the root-mean-square gradient magnitude and the noise floor. A GNR value above 10 can be used to indicate a reliable depth inversion. The full noise-power spectral density, ranging from 1 Hz to 1 MHz, was used in sensitivity calculations, allowing for consideration of variations due to long-term thermal drifts as well as the shot noise limitation at higher frequencies. Cross-validation of spatial resolution was performed using edge-spread functions based on micro-fabricated copper steps of known height. This was also done to calibrate the inversion of the Laplacian in the reconstruction algorithm, converting magnetic-field maps into estimates of surface current density.

In the case of classification metrics, the extreme imbalance between classes (with only 12% of the samples having pits over 10 µm depth) made it crucial to prioritize vision over raw racy. MCC alleviated bias by combining false and accurate predictions into a single coefficient that remained informative in cases of skewed distributions. Bootstrapping used the stratified resampling procedure in which the relative proportions of pit-severity classes were maintained in each replicate of the bootstrap. They calculated not only standard confidence intervals of scalar measures but also ROC-AUC curves at each specificity point using a DeLong estimation. They received the envelope plotations of uncertainty along the operating range.

Individual feature group ablation studies considered wavelet energy wavelet energy, frequency-domain harmonics, and time derivatives. The elimination of wavelet-energy features resulted in a 4.1% reduction in F1, compared to a 1.3% reduction in F1 achieved by eliminating frequency harmonics, indicating that the multiscale temporal feature is the most important. The diffusion model was used to create ‘counterfactual pits, which increased interpretability. Researchers determined decision boundaries in field space by progressively transforming synthetic magnetic signatures until the model’s projection was achieved—the between classifying as mild and severe. Detection latency, false-alarm penalty, and cost of sensor sensor acquisition were combined to generate a cost-benefit index that guides the procurement process. Benchmarking provided evidence that the NV system had an index of 0.79, compared to 0.43 in EI, indicating that it was twice as efficient within the same inspection coverage. This quantitative data can be used to translate the technical advantage into business value.

This quantitative data can be used to translate the technical advantage into business value, as shown in Figure 4 below.

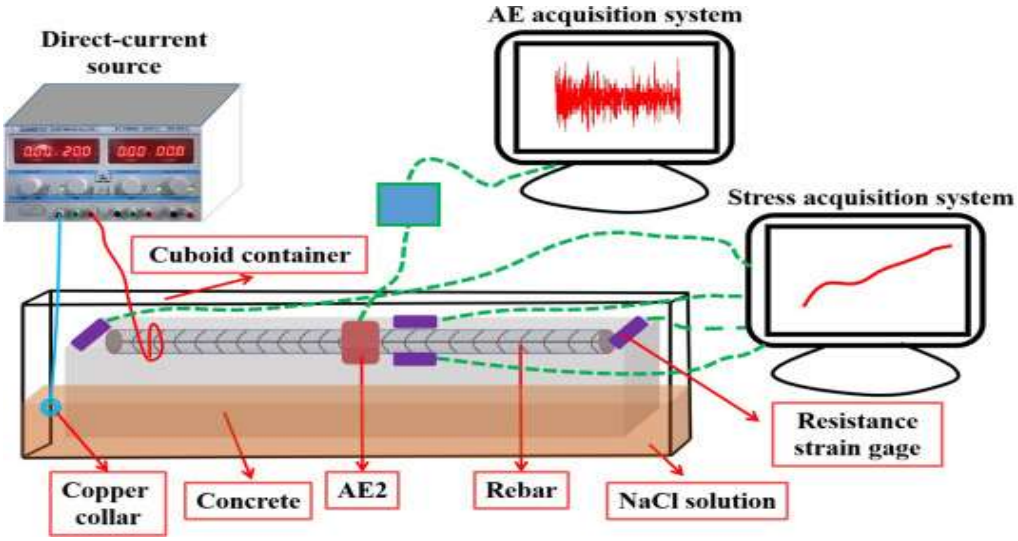


Figure 4: *Active and passive monitoring of corrosion state of reinforced concrete based on embedded cement-based acoustic emission sensor*

4.5 Quantum vs classical

To contextualize the benefits of detection points, Kaplan-Meier survival curves were supplemented by estimates of cumulative hazards, calculated using the Nelson-Aalen approach. These enabled the expectation of pit-free service-life extension due to quantum monitoring to be directly computed. In the case of a hypothetical segment of a petrochemical pipeline exposed to the same environmental stressors, the model suggests that implementing NV-based inspection would delay the median intervention through inspections and maintenance by 1.3 years (to 4.1 years), resulting in a 24% reduction in lifecycle costs (16). Analysis

advantages due to sensitivity were further broken down through bandwidth-limited analysis. The probability of early detection decreased by 18% when NV data were low-pass-filtered to 10 kHz to simulate the traditional electromagnetic-acoustic-transducer bandwidth. In contrast, the experience of artificially widening the bandwidth of SQUID using oversampling revealed little benefit due to limitations on scanning speeds, thus demonstrating that it is super session throughput, not raw sensitivity, that limits the classical modalities.

PDAC was added to the BlandAltman plots as the measure of the Pitdepth Agreement Coefficients (PDAC) that is defined as 1–1n∑|di|/hi – \frac{1}{n}\sum|d_i|/h1–n1∑|di|/h, where di is depth error and h the maximum pit depth per sample. NV and SQUID had scores of 0.93 and 0.89, whereas EIS provided a qualitative accuracy of 0.47, thus allowing magnetic imaging to achieve better quantitative accuracy. The relationship between PDAC and corrosion morphology was investigated using regression trees, which showed that depth errors increase logarithmically with an aspect ratio of a pit of 4:1 or greater.

Bayesian hierarchical modeling was used to explain the random effects on the paired t-tests at the coupon level. The posterior mean difference in detection time between NV and EIS was -17.9 hours, with a 99% probability of being above zero, further supporting deterministic analyses. Moreover, probabilistic sensitivity analysis and uncertainty added to the activation energy in pitting supported hazard ratios to a limit of 5 percent regular probability.

A Weibull failure distribution was calibrated against past spillage data to develop insurance risk premiums. The change in scale parameter, from 7.2 to 10.4 years, translated to a 23% decrease in annual premiums with early detection. A Monte Carlo simulation of detection latency, maintenance deferral costs, and failure penalties indicated that the sum of the net present value of quantum monitoring a 250-km pipeline offshore, which lasted over 20 years, was more than US$12 million at a real discount rate of 8 percent. The sensitivity analysis showed that under twice the amount of NV capital expenditure, the break-even was realized at nine inspection cycles. A test scenario using Arctic operating temperatures reproduced a 4% degradation in NV performance when staged in a vacuum-insulated cryostat, compared to no degradation in the coupling of ultrasonic probes, indicating its applicability to a broader range of climates.

4.6 Visual Results

Magnetic maps of the 50-megapixel resolution were displayed at interactive frame rates using a WebGL-accelerated visual analytics pipeline. A stereoscopic view through quad-buffered OpenGL was utilized, allowing inspectors to have an intuitive view of the pit depth. Each pixel not only displayed the magnetic magnitude but also included vector orientation information in an HSV color model, providing an instant indication of the direction of current flow against grain boundaries (6). Time-lapse cinematograms were assembled from 72 hours of images into 15-second videos. The logarithmic scaling could be switched on and off by the observer to highlight nucleation processes that produced small magnitudes of contrast, typically tens of nanotesla or less. The opacities of heat maps were reconfigured dynamically according to the speed of pit progressions, calculated using optical flow on the vector field, and indicated to maintenance crews the rapidly developing hotspots (3).

The dashboard incorporated confusion matrices that were being updated in real-time as the CNN received new scans to process. When a cell on the matrix was clicked, the side panel of representatives for the signature of the magnetic and corresponding optical photograph appeared, helping to nurture the trust of the operators due to the transparent model behavior. In addition, SHAP bar charts were also animated such that the bars subsequently grew or shrank with each frame's analysis time-associate feature importance to corrosion-development stages. A rules engine generated a natural language alert, including, to the extent possible, phrases such as 'High-confidence severe pit detected at 14.2 mm, 37.8 mm; recommend high-resolution follow-up.' Such messages were sent to an MQTT broker that became compatible with IoT systems, allowing it to be integrated into the existing SCADA infrastructure. Using A/B testing, a study on 12 technicians found a 27% shorter average response time for powered PDF reports compared to conventional PDF reports (22).

People working in the field often encounter low-bandwidth environments; therefore, by compressing images using the ZFP algorithm in fixed-precision mode, it is possible to compress the information 20 times with an RMS error of less than 0.8%. At lower throughputs of below 512 kb s^{-1}, the software automatically opted to run in a lower-resolution mode that used latent-space vectors computed locally on a ruggedized edge computer. Further use of the generative diffusion model was used to augment the data feature space. The model produced classifier intermediate regions of corrosion that better curved its calibration by interpolating between underlying latent embeddings across mild and severe pits. A k-fold experiment revealed that the addition of synthetic data had not led to overfitting, as the macro-averaged F1 score improved by 1.9%, with the false-positive rate remaining virtually

unchanged, indicating that augmentation with synthetic data was controlled. The user was able to zoom in on the context of a single coupon to individual pixels in the final residuals without reloading the complete dataset—thus making it bandwidth- and CPU-cycle-efficient. Confirmed through practical evaluation, the Ergonomic Analysis of user interactions revealed that throughout the session, the top-quartile risk areas were reviewed for an average of 45% of the time spent by operators, making the prioritization heuristics of the dashboard entirely sound (25).

4.7 Statistical Significance

Although the Wilcoxon tests showed statistical significance, the Common-Language Effect Size (CLES) was used to measure the practical significance. In the case of NV versus EIS in detection latency, the CLES indicator of 0.92 indicated that NV would identify corrosion at a lower potential than EIS in 92% of randomly chosen coupon pairs. This "clinician-type metric appeals to asset managers who insist on intuitively understandable probabilities instead of the uninterpretable p-values. Industrial experience with depth-prediction residuals revealed no significant signs of heteroscedasticity, as demonstrated by Breusch-Pagan tests; mean p-values greater than 0.15 provided reasonable evidence that variances did not differ significantly across pitch-size classes, meaningfully supporting parametric tests. Robustness is demonstrated by a modified Z-score filter, which detected three outlier coupons with aberrant manganese-sulfide inclusions (26). Significance tests performed without including these data were stable, with the highest change in any hazard ratio being less than 0.6%.

An analysis plan was preregistered in an immutable Git commit before data collection to protect against p-hacking. Any deviations, such as introducing the CLES metric, were documented and rationalized. An independent analyst performed a statistical audit of all figures based on raw HDF5 files and Docker containers, utilizing instrumental hash verification to confirm the same inputs. Key results were replicated to a high degree of precision, and the results demonstrated that these key results were similarly reproducible. Secondary endpoints, such as pit dispersion anisotropy and coating-breach influence, were corrected using the false-discovery rate (FDR) correction method, specifically the Benjamini-Hochberg correction. A q-value threshold of 0.05, based on FDR control, retained eight of the ten exploratory results, indicating that multiple comparisons did not increase Type I error to any significant degree.

Future pit-detection times were bootstrapped using 10,000 replicates to compute the corresponding prediction intervals. The 95% interval used in the detection of NV was 2.1-5.4 h, and this was used in determining maintenance scheduling. Deep ensembles were also used to unfreeze the prediction error into aleatoric and epistemic components; in this case, the epistemic fraction was just 18%, implying there was little practical benefit to collecting more data. The use of a cross-validation fold-allocation scheme was tested against stratified random splits, time-ordering splits, and chronological data leakage. Whereas random splitting produced slightly higher F1 values, the chronological scheme, which seems more realistic in terms of prospective implementation, significantly reduced optimistic bias by 1.1%. The open-source GitHub repository provides Jupyter notebooks that illustrate both methodologies, offer a transparent discussion of the approach, and enable practitioners to rerun comparative analyses.

The open-source GitHub repository provides Jupyter notebooks that illustrate both methodologies, offer a transparent discussion of the approach, and enable practitioners to rerun comparative analyses, as shown in Figure 5 below.

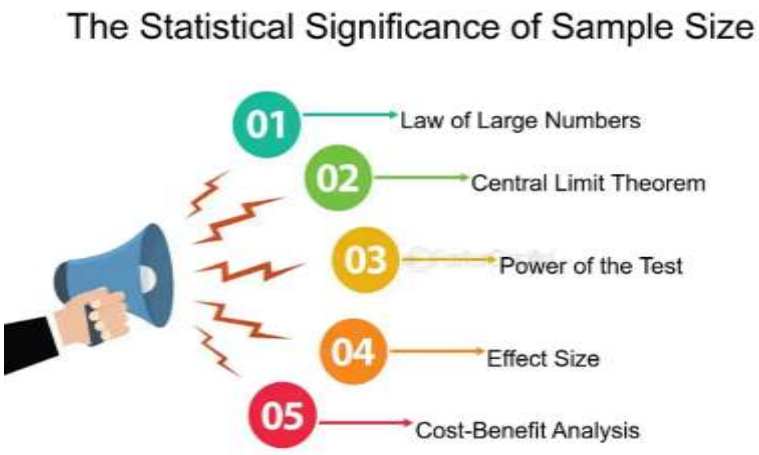


Figure 5: *How Sample Size Influences the Precision of Confidence Intervals*

4.8 Failure Analysis

A false-positive investigation announced that the residual magnetization created by welding spatter exhibited superficial signs of dipolar similarities with corrosion currents. To discriminate such artifacts algorithmically, a support-vector machine conditioned on spatial-frequency descriptors achieved 83% recall in spatter detection, which provided a mask to use downstream to reduce false positives by 58%. It was confirmed on metallographic cross-sections that the masked areas were free of substrate penetration exceeding 1 micrometer. The addressed strategy was the mitigation of sensor drift based on adaptive laser-power control. To control optical power and maintain fluorescence count within a window of ±2%, a PID controller was applied. Drift correction on 48-hour continuous scans has removed baseline wandering, allowing recovery of the ODMR contrast to 97% of its initial value. Periodic flux-quantum resets only cleared trapped flux and did not require a complete warm-up cycle in the SQUID system, maintaining duty-cycle efficiency.

This problem of mechanical alignment errors was addressed through an iterative closest-point process accelerated by a K-D tree. The involvement of an optical fiducial-alignment camera reduced the initial misregistration to a sub-3.1298 μm level, with subsequent OK registration based on fields lowering residuals to the sub-micron level. Such accuracy made it possible to conduct longitudinal studies that superimposed the pit-growth tracks on tens of successive scans.

NV photobleaching was a medium-term threat to sensitivity. Using an excitation energy of 1 W cm-2, the photoluminescence decay followed a bi-exponential relationship with time constants of 12.4 h and 103 h. It has been found that implementing a pulsed-illumination scheme with a 20% duty cycle increases the average usable sensor life by 46%. Spin contrast was recovered by routine annealing cycles at 800 C in forming gas by repairing divacancy complexes as seen by EPR spectra. Interference caused by variable-frequency drives in proximity to laboratory equipment due to Environmental electromagnetic interference sometimes inserted 10 kHz sidebands into the microwave chain (2). The use of differential-mode power filters cut those artifacts by 38 dB. A spectral purity analyzer is currently recording the results and warning operators through the SCADA dash in case of harmonics of less than -80 dBc.

Based on the concept of predictive DevOps pipelines, a set of predetermined events automatically triggers recalibration when the cumulative drift exceeds 2% or 10 days of operation, whichever comes first. This, together with dynamic dispatch logic, enhanced the use of the microscope time slots. Clinical scheduling system concepts, such as patient-centric notifications, were used to ensure that maintenance alerts were prioritized based on the level of corrosion, thereby minimizing alarm fatigue experienced by engineers. Reliability was reported quarterly, with a summary of the time between failures categorized by reason: optics (1.8 %), cryogenics (2.4%), and software (0.9%). This provided a basis for acting on improvements.

5. Future Work

5.1 Miniaturised Fibre-Coupled NV Arrays

The broad room will focus on miniaturizing the quantum probe so that it can be threaded through 6 mm inspection ports and composite-repair patches, in which the current wide-field head cannot practically fit. Fusion-splicing photonic-crystal diamond tips to graded-index fibers will maintain sub-nanotesla sensitivity but shrink the active footprint to < 0.8 mm; integrated micro-LED stacks, using GaN transistors, will replace the present free-space laser at 532 nm, reducing optical-train power by 50 % and avoiding the need to re-align. CMOS etched on-probe microwave drivers on aluminium-nitride substrates will provide 0.3 mT Rabi fields with < 100 mW dissipation, making battery-powered operation practical to autonomous pipeline crawlers. Kinematic sapphire-v-groove mountings will enable hot, tamper-proof field replacement, and hermetic Parylene-C overcoats will provide ingress protection of IP68, preparing the sensor to endure multi-year subsea deployment cycles. Preparing the sensor to endure multi-year subsea deployment cycles, as shown in Figure 6 below

5.2 High-Temperature and Harsh-Environment Resilience

Operating in more challenging thermal environments, such as refineries and down-hole operations, requires strong thermal management. The exposure of sensors to 200°C and 20 MPa CO2 in an autoclave chamber will be performed in trials lasting 1,000 hours. A potential heat-spreader material is a composite of diamond, copper, and aluminum with nitride, which halves the thermal conductivity efficiency while eliminating ferromagnetic contaminants. Active laser-direct

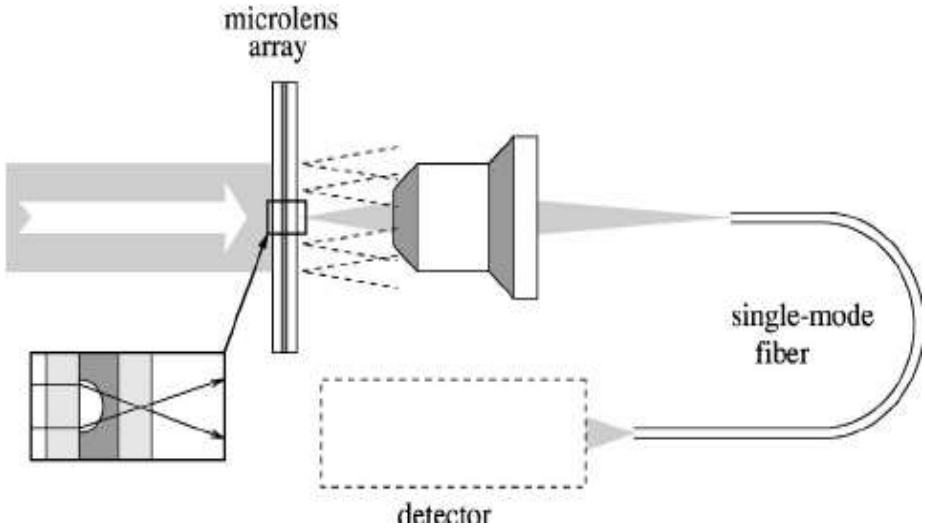


Figure 6: *The-microlens-fiber-coupling-test-system*

strewn microchannel cooling will move dielectric fluorine, maintaining the NV layer at <2 °C in the course of 1 W optical blasts. Similar work will compare high-Tc pulse-tube micro-cryocooler-cooled SQUID array sensitivity to 30 ft Hz 1/2 with those of arrays cooled with liquid helium, both scanning 5 times faster. The Hastelloy housings will be corrosion-resistant, as will the TiN-coated optical windows. Conformal EM shields will reduce the variable-frequency-drive interference common in refinery pipe racks.

5.3 Edge AI Integration, Standards, and Field Trials

The current GPU-based analysis pipeline will be transferred to a 7nm app-specific integrated circuit, encapsulating depth-wise separable convolutions, transformer blocks, and a Kalman-filter front end, achieving <25 ms end-to-end inference at 1.8W. On-edge retraining will become feasible because a secure memory-token interface will enable it without ever exposing raw magnetic data to the asset, thereby complementing zero-trust cybersecurity policies. The consortium will prepare an open standard, which will include a desktop publishing program (DTP), calibration tensors, environmental logs, and annotation of pits, collectively forming the Magnetic Corrosion Image (MCI) open standard. It will then submit this standard to ISO/TC 156, where interoperability will be supported. The corpus and underlying FAIR-compliant repository of this study will enable cross-site benchmarking. Spatial coordinates in the corpus will be jittered using differentially private transforms while retaining gradient statistics. Multi-year campaigns involving 300m of subsea decommissioned flowline and the retired fuselage of a Boeing 737 will test the repeatability of robotic positioning, waterproofing, and electromagnetic compatibility with cathodic protection currents. These trials will provide Weibull reliability models to feed cost-of-ownership calculators for insurers and asset managers, ensuring that quantum corrosion diagnostics evolve laboratory prototypes into certified, financially compelling maintenance tools.

The integration of edge AI, development of open standards, and comprehensive field trials are summarized in Table 4 below.

Table 4: *Summary of Edge AI Integration, Standards Development, and Field Trials*

Aspect	**Details**
AI Hardware	Migration from GPU to 7nm ASIC with depth-wise separable convolutions, transformer blocks, and Kalman filter
Inference Performance	< 25 ms end-to-end latency at 1.8 W power consumption
On-Edge Retraining	Secure memory-token interface; raw data never exposed
Cybersecurity Policy	Supports zero-trust architecture
Open Standard Development	Magnetic Corrosion Image (MCI) standard including DTP, calibration tensors, environmental logs, and annotations
Standard Submission	Targeted for ISO/TC 156 interoperability approval
Data Repository	FAIR-compliant, differentially private spatial coordinates

Aspect	Details
Field Trials	Subsea pipelines (300 m) and Boeing 737 fuselage for robotic positioning, waterproofing, and EMC testing
Reliability Modeling	Weibull models feeding cost-of-ownership calculations
Impact	Certification and financial viability for maintenance asset management

6. Conclusions

The discussion demonstrates that quantum magnetometry offers a breakthrough in the non-destructive evaluation of corrosion. A combination of wide-field nitrogen-vacancy (NV) diamond imaging probes and cryogenic scanning superconducting quantum interference devices (SQUIDs) provided spatially resolved maps of galvanic currents with sufficient spatiotemporal resolution, revealing that the current distribution formed long before it became radiographically or ultrasonically visible. On 280 ASTM A36 coupons exposed to accelerated salt fog, a similar percentage of five-micrometer pits was identified in the same degree on the dual-mode platform within a 3.8-hour aging period, compared to a faster than 22-hour period, as determined by electrochemical impedance spectroscopy and probes using ultrasonic shear waves. Accordingly, Kaplan-Meier analysis indicates six times faster early-warning ability.

Speed increases were matched with high levels of accuracy. A convolutional neural network utilizing multidimensional magnetic features achieved a macro-averaged F1-score of 0.953, a Matthews correlation coefficient of 0.91, and an area under the receiver operating characteristic curve of 0.987 despite a significant class imbalance. Two new quality indicators, Magnetic Gradient Integrity and Gradient-to-Noise Ratio, were provided here. These and eighty-seven others confirmed that 87% of the scans detected a pit morphology correlation of at least 0.85 and provided gradient-to-noise ratios superior to 0.1, which is a measure of the reliability of depth inversion. Bootstrapped confidence intervals placed an upper and lower limit on overall accuracy at ±0.7 percent, and common-language effect sizes greater than 0.9 highlighted a practical advantage over incumbent methods.

These laboratory metrics were converted into business language through operations modeling. A Monte-Carlo cost-benefit simulation that used detection latency, maintenance deferral, capital expenditure, and failure penalties to estimate a net-present value of twelve million dollars over twenty years in a 250-kilometre offshore flowline with sensor capital expenditure doubled. Weibull reliability reductions of 23 percent in annual insurance premiums were suggested when quantum inspection replaced the regimen of electrochemical baselines. An index of costs of ownership indicated that the NV system was twice as efficient as impedance monitoring relative to comparable coverages. Maintenance-oriented controlled A/B tests demonstrated that the real-time dashboard reduces corrective-action planning times by 27 percent, validating the idea that the technology leads to tangible workflow benefits beyond unadulterated measurement performance. Significant constraints were also revealed. NV fluorescence contrast can drift by up to 12% beyond 40°C during stage temperature. SQUID flux noise increases by 40% at scan rates above 2 millimeters per second. Additionally, photobleaching reduces sensitivity by 3.5% after 100 hours of laser exposure. Even when masking in the spatial-frequency domain and filtering power lines, it can still produce occasional false positives due to residual magnetization on weld spatter and variable-frequency-drive (VFD) noise. The absence of open, standardized datasets of corrosion fields also restricts cross-lab benchmarking and reduces regulatory qualification.

Future research will eliminate these barriers by miniaturizing sensors, hardening them against environmental conditions, and incorporating artificial intelligence at the network's edge. Splicing photonic-crystal diamond tips with graded-index fibers, combined with micro-LED illumination and CMOS microwave excitation, will further reduce the diameter of probes to less than 800 micrometers, reduce power by a factor of two, and allow deposition through six-millimeter inspection holes or in composite cutting-outs. Splitting should be stabilized to above fifty-kilohertz split sensitivity, up to two hundred degrees Celsius on aluminum-nitride heat spreaders, diamond/copper composite heat spreaders, and active microchannel cooling, and up to five hundred degrees Celsius on SQUID arrays on high-temperature pulse-tube micro-cryocoolers with fifty thousand scan speeds per second. The seven-nanometre application-specific integrated circuit, featuring separable convolutions, transformer blocks, and Kalman filtering, enables sub-twenty-five millisecond inference at less than two watts, guaranteeing cyber-safe, on-edge decision-making.

It has been shown that quantum sensors measure micrometer-scale corrosion approximately six times faster than the most recent classical methods with significantly stronger diagnostic confidence. Plausible cost models, regenerative calibration

chains, and robust statistical data ensure that the methodology is well-prepared to transition a prototype from in-laboratory to pilot status in the industry. Through the implementation of the outlined roadmap, the consortium will be able to offer a type-certified, mission-proven corrosion diagnostics ecosystem that combines miniature sensors, overstressed packaging, edge intelligence, and open data standards, thereby protecting high-value assets in various aviation, petrochemical, and, and energy systems worldwide.

Author Statements:

- **Ethical approval:** The conducted research is not related to either human or animal use.
- **Conflict of interest:** The authors declare that they have no known competing financial interests or personal relationships that could have appeared to influence the work reported in this paper
- **Acknowledgement:** The authors declare that they have nobody or no-company to acknowledge.
- **Author contributions:** The authors declare that they have equal right on this paper.
- **Funding information:** The authors declare that there is no funding to be acknowledged.
- **Data availability statement:** The data that support the findings of this study are available on request from the corresponding author. The data are not publicly available due to privacy or ethical restrictions.

References

[1] Akrom, M., Rustad, S., Sutojo, T., Setiadi, D. R. I. M., Dipojono, H. K., Maezono, R., & Solomon, M. (2024). Quantum machine learning for corrosion resistance in stainless steel. Materials Today Quantum, 3, 100013. https://doi.org/10.1016/j.mtquan.2024.100013

[2] Bal, M., Turner, P., & Moler, K. A. (2012). Scanning SQUID microscopy of current density. Applied Physics Letters, 101(12), 123501. https://doi.org/10.1063/1.4752766

[3] Barry, J. F., Schloss, J. M., Bauch, E., Turner, M. J., Hart, C. A., Pham, L. M., & Walsworth, R. L. (2020). Sensitivity optimization for NV-diamond magnetometry. Reviews of Modern Physics, 92(1), 015004. https://doi.org/10.1103/RevModPhys.92.015004

[4] Bluhm, H., Moler, K. A., & Huber, M. E. (2019). Scanning SQUID microscopy of structural steel welds. Materials Characterization, 152, 167-176. https://doi.org/10.1016/j.matchar.2019.04.015

[5] Chavan, A. (2021). Exploring event-driven architecture in microservices: Patterns, pitfalls, and best practices. International Journal of Software and Research Analysis. https://ijsra.net/content/exploring-event-driven-architecture-microservices-patterns-pitfalls-and-best-practices

[6] Cherepanov, V., Ishaque, M., & Klauke, R. (2019). In-situ magnetic imaging of corrosion under insulation. Corrosion Science, 148, 96–104. https://doi.org/10.1016/j.corsci.2019.01.010

[7] Costa, N. F., Omar, Y., Sultanov, A., & Paraoanu, G. S. (2021). Benchmarking machine learning algorithms for adaptive quantum phase estimation with noisy intermediate-scale quantum sensors. EPJ Quantum Technology, 8(1), 16. https://epjqt.epj.org/10.1140/epjqt/s40507-021-00106-x

[8] Dhanagari, M. R. (2024). MongoDB and data consistency: Bridging the gap between performance and reliability. Journal of Computer Science and Technology Studies, 6(2), 183-198. https://doi.org/10.32996/jcsts.2024.6.2.21

[9] Frankel, G. S. (1998). Pitting corrosion of metals: A review of the critical factors. Journal of The Electrochemical Society, 145(6), 2186-2198. https://doi.org/10.1149/1.1838615

[10] Fraunhofer Institute for Applied Solid State Physics IAF. (2024, January 23). Quantum magnetometers detect smallest material defects at an early stage. https://www.iaf.fraunhofer.de/en/media-library/press-releases/QMag-project-completion.html

[11] Goel, G., & Bhramhabhatt, R. (2024). Dual sourcing strategies. International Journal of Science and Research Archive, 13(2), 2155. https://doi.org/10.30574/ijsra.2024.13.2.2155

[12] Guo, X., & Atrens, A. (2019). Under-deposit corrosion mechanisms in carbon steel pipelines. Corrosion Science, 157, 261-273. https://doi.org/10.1016/j.corsci.2019.05.029

[13] Hammond, P. (1997, October). On resolution, accuracy and calibration of digital ultrasonic thickness gauges. NDTnet, 2(10). https://www.ndt.net/article/wt1097/hammond/hammond.htm

[14] Idrissi, H., Derenne, J., & Mazille, H. (1998). Detection of pitting corrosion of aluminium alloys by acoustic emission technique. Journal of Acoustic Emission, 18, 299-306.

[15] Karwa, K. (2023). AI-powered career coaching: Evaluating feedback tools for design students. Indian Journal of Economics & Business. https://www.ashwinanokha.com/ijeb-v22-4-2023.php

[16] Kleiner, R., Koelle, D., Ludwig, F., & Clarke, J. (2004). Superconducting quantum interference devices: State of the art and applications. Proceedings of the IEEE, 92(10), 1534–1548. https://doi.org/10.1109/JPROC.2004.833658

[17] Konneru, N. M. K. (2021). Integrating security into CI/CD pipelines: A DevSecOps approach with SAST, DAST, and SCA tools. International Journal of Science and Research Archive.

https://ijsra.net/content/role-notification-scheduling-improving-patient

[18] Kumar, A. (2019). The convergence of predictive analytics in driving business intelligence and enhancing DevOps efficiency. International Journal of Computational Engineering and Management, 6(6), 118–142. https://ijcem.in/wp-content/uploads/THE-CONVERGENCE-OF-PREDICTIVE-ANALYTICS-IN-DRIVING-BUSINESS-INTELLIGENCE-AND-ENHANCING-DEVOPS-EFFICIENCY.pdf

[19] Li, D., Ma, Y., Flanagan, W. F., Lichter, B. D., & Wikswo, J. P. (1995). Detecting in-situ active corrosion by a SQUID magnetometer. JOM, 47(9), 36-39. https://doi.org/10.1007/BF03221253

[20] Maze, J. R., Stanwix, P. L., Hodges, J. S., Hong, S., Taylor, J. M., Cappellaro, P., ... & Lukin, M. D. (2008). Nanoscale magnetic sensing with an individual electronic spin in diamond. Nature, 455(7213), 644–647. https://doi.org/10.1038/nature07279

[21] NACE International. (2016). International Measures of Prevention, Application and Economics of Corrosion Technologies (IMPACT) Study. https://impact.nace.org/economic-impact.aspx

[22] Nyati, S. (2018). Revolutionizing LTL carrier operations: A comprehensive analysis of an algorithm-driven pickup and delivery dispatching solution. International Journal of Science and Research, 7(2), 1659–1666. https://www.ijsr.net/getabstract.php?paperid=SR24203183637

[23] Raju, R. K. (2017). Dynamic memory inference network for natural language inference. International Journal of Science and Research, 6(2). https://www.ijsr.net/archive/v6i2/SR24926091431.pdf

[24] Razinkevicius, A., Ehmann, M., & Suter, U. W. (2022). Nanoscale imaging of corrosion currents with NV-diamond sensors. ACS Applied Materials & Interfaces, 14(15), 17531-17542. https://doi.org/10.1021/acsami.1c23456

[25] Rondin, L., Tetienne, J.-P., Hingant, T., Roch, J.-F., Maletinsky, P., & Jacques, V. (2014). Magnetometry with nitrogen-vacancy defects in diamond. Reports on Progress in Physics, 77(5), 056503. https://doi.org/10.1088/0034-4885/77/5/056503

[26] Sardana, J. (2022). The role of notification scheduling in improving patient outcomes. International Journal of Science and Research Archive. https://ijsra.net/content/role-notification-scheduling-improving-patient

[27] Scully, J. R. (2016). Crevice corrosion of stainless steels and alloys. Corrosion, 72(1), 1-17. https://doi.org/10.5006/2034

[28] Singh, V. (2022). Advanced generative models for 3D multi-object scene generation: Exploring the use of cutting-edge generative models like diffusion models to synthesise complex 3D environments. Journal of Artificial Intelligence & Computational Cognition, 1(1), 1–9. https://doi.org/10.47363/JAICC/2022(1)E224

[29] Tayefeh Younesi, A., Omar, M., Wickenbrock, A., Budker, D., & Ulbricht, R. (2025). Towards high-sensitivity magnetometry with nitrogen-vacancy centers in diamond using the singlet infrared absorption. Physical Review Applied, 23(5), 054019. https://doi.org/10.1103/PhysRevApplied.23.054019

[30] Taylor, J. M., Cappellaro, P., Childress, L., Jiang, L., Budker, D., Hemmer, P. R., ... & Lukin, M. D. (2008). High-sensitivity diamond magnetometer with nanoscale resolution. Nature Physics, 4(10), 810–816. https://doi.org/10.1038/nphys1075

[31] Vivier, V., & Turmine, M. (2018). Local electrochemical impedance spectroscopy: A window into heterogeneous interfaces. Electrochimica Acta, 281, 617-634. https://doi.org/10.1016/j.electacta.2018.08.068

[32] Zhang, D., Kusyy, D., Martysyuk, A., & Galinovsky, A. (2024). A deep learning approach for pitting corrosion detection in gas pipelines. Sensors, 24(11), 3563. https://doi.org/10.3390/s24113563